Evaluation of the vortex core size in gate-tunable Josephson junctions in Corbino geometry

Sadashige Matsuo [1,2,3,*] Mizuki Tateno,[1] Yosuke Sato [1] Kento Ueda,[1] Yuusuke Takeshige,[1] Hiroshi Kamata [1,3]
Joon Sue Lee [4] Borzoyeh Shojaei,[5] Christopher J. Palmstrøm [4,5,6] and Seigo Tarucha[1,3,†]

[1]*Department of Applied Physics, The University of Tokyo, 7-3-1 Hongo, Bunkyo-ku, Tokyo 113-8656, Japan*
[2]*JST, PRESTO, 4-1-8 Honcho, Kawaguchi, Saitama 332-0012, Japan*
[3]*Center for Emergent Matter Science, RIKEN, 2-1 Hirosawa, Wako-shi, Saitama 351-0198, Japan*
[4]*California NanoSystems Institute, University of California, Santa Barbara, California 93106, USA*
[5]*Materials Department, University of California, Santa Barbara, California 93106, USA*
[6]*Electrical and Computer Engineering, University of California, Santa Barbara, California 93106, USA*

We report on electron transport in gate-tunable Corbino-geometry Josephson junctions (CJJs) fabricated from an epitaxially grown Aluminum (Al) superconductor on an InAs quantum well. We observed that a supercurrent can be tuned by the gate voltage and sweeping an out-of-plane magnetic field initiates a sudden rise in the electrical resistance. From the analysis using a theoretical model for flow resistance due to Josephson vortices in CJJs, we evaluate the vortex core size, which substantially depends on the carrier density and temperature. These results will be subsequently utilized for future operations of the Josephson vortices in CJJs.

The superconducting correlation in two superconductors is weakly linked by the Josephson effect through thin insulators or metals [1,2]. In particular, when a normal metal connects two superconductors, the superconducting correlation penetrates into the normal metal owing to the superconducting proximity effect. The critical current through long rectangular Josephson junctions oscillates with magnetic fields, generating a Fraunhofer diffraction pattern [3]. This response can be explained using the entries of Josephson vortices [4–6] into the junction. Josephson vortices are analogous to Abrikosov vortices in type-II superconductors [2,7]. Recently, interest in the Josephson vortices has been revived because some theories have proposed a Majorana fermion (MF) as a localized state at the center of the vortex in proximity-induced superconductivity in topological insulators [8–12].

A strategy for electrical control and evaluation of Josephson vortices is to utilize a Corbino-geometry Josephson junction (CJJ); a circular junction between the inner and outer superconducting electrodes. The vortices in a CJJ should be confined in the junction. Additionally, the vortices can be driven by an electric current via the Lorentz force which enables them to swap positions [13,14]. Some theoretical studies propose the braiding operation of MFs using CJJs of topological insulators based on the electrical control of the Josephson vortices [15–17]. The real-space structure of the core was previously observed by a scanning tunnel microscope measurement in a Pb island junction [6]. Additionally, the vortices in the planar Josephson junction have been studied in electron transport using magnetic force microscopy [18]. However, there is only one experimental report of the supercurrent and its magnetic field dependence in CJJs of Nb/Cu/Nb [13] while

the normal electron transport in the Corbino geometry devices have sufficiently been studied experimentally [19–22]. Further studies are necessary to reveal the superconducting transport in CJJs and control the vortices in them. Evaluation of the properties of Josephson vortices in CJJs will provide important information which can later be used in topologically nontrivial systems to study the MFs in the vortex cores.

Here, we show the experimental results of gate-tunable CJJs fabricated in a heterostructure of epitaxially grown thin aluminum (Al) film/InAs quantum well. We succeeded in the gate tuning of the supercurrent flowing through the CJJs. We observe that the supercurrent suddenly disappears, and a finite resistance emerges when the magnetic field is swept from zero. The emergence of the resistance can be explained using a theoretical model of flow resistance of the vortices. Thereafter, we evaluate the core size from the magnetic field dependence of the resistance and the obtained results strongly depended on the gate voltage and temperature. Our results imply that operations on the Josephson vortices may, in future, be achieved through gate and temperature control.

The device studied is fabricated from an epitaxially grown 10-nm-thick Al film on InGaAs/InAs (two-dimensional electron gas)/InGaAs/InAlAs on an InP substrate, which gives a highly transparent interface between Al and the two-dimensional electron gas [23–25]. Using selective wet etching, we first formed circular junctions which define an inner Al electrode and an outer Al electrode. The schematic image of the top view of the circular junction is shown in the lower panel of Fig. 1(a). The fabricated circular junction has a 100-nm gap between the two Al electrodes and a radii of 10 μm. Carrier density n of the InAs quantum well after removing the Al layer is $n = 9.0 \times 10^{11}$ /cm^2 [26]. We thereafter cover the device with cross-linked polymethyl methacrylate (PMMA) [27] except at the center of the inner Al electrode.
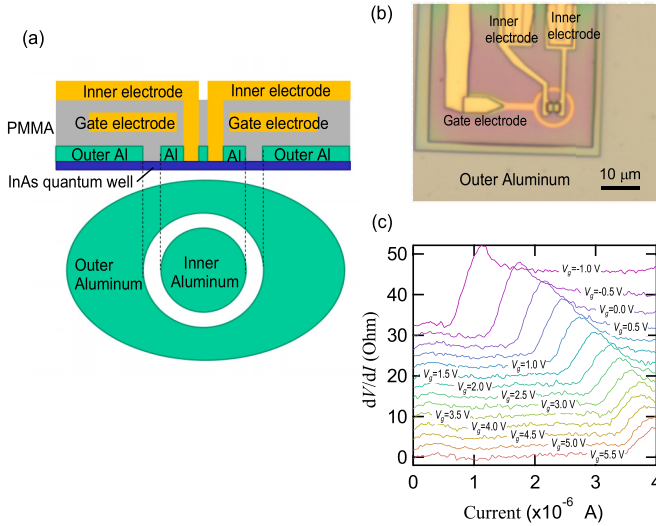
FIG. 1. (a) A schematic image of the cross section of the fabricated CJJ is shown in the upper panel. The view from above is in the lower panel. (b) An optical image of the CJJ. The scale bar is 10 μm. (c) The differential resistance at 0.3 K as a function of bias current at several V_g in the range of -1.0 V $< V_g < 5.5$ V. The y axis shows the data for $V_g = 5.5$ V; the other data are incremented upward by 2.5 Ω. The supercurrent region shrinks as V_g reduces.
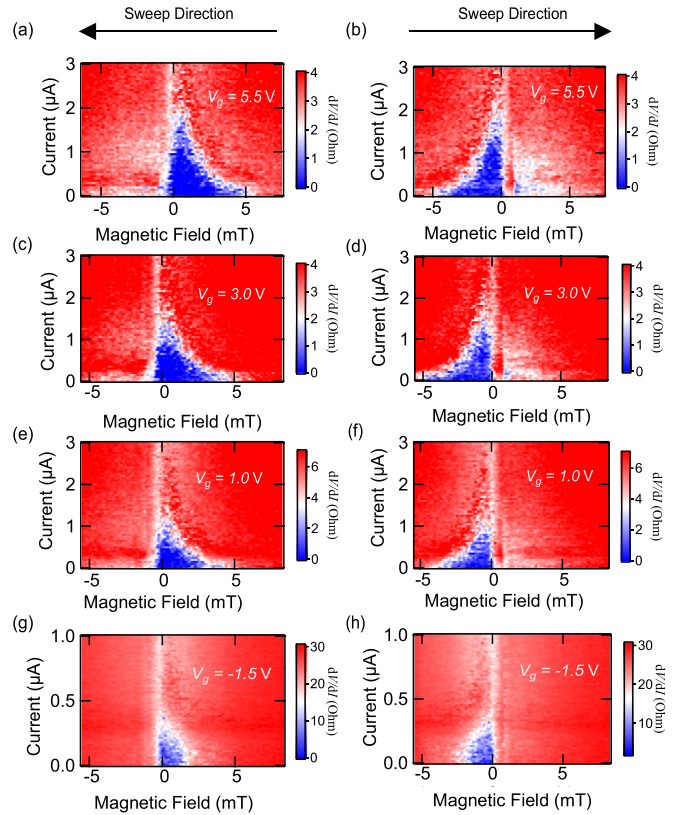

FIG. 2. (a) dV/dI as a function of magnetic fields and bias current when the magnetic field is swept from 9 to -6 mT. This result is obtained at $V_g = 5.5$ V. (b) The same as (a), except for the sweep direction. (c),(e), and (g) indicate dV/dI at $V_g = 3.0$ V, 1.0 V, and -1.5 V, respectively, when the magnetic field is swept from 9 to -6 mT. (d), (f), and (h) indicate the same as (c), (e), and (g) with the opposite sweep direction.

The gate electrode of Ti/Au is fabricated atop this first crosslinked PMMA layer. Next, we again coated the crosslinked PMMA on the gate electrode. Finally, we made two Ohmic contacts on the center of the inner Al electrode through the contact on the two-dimensional electron gas where there is no cross-linked PMMA. A schematic image of the cross section of the fabricated CJJ is shown in the upper panel of Fig. 1(a). As for the outer electrode, the wire bonding was performed on the Al pads connected to the outer electrode. An optical image of the real fabricated device is shown in Fig. 1(b). This characteristic structure permits the measurement of the electron transport in the CJJ using a four-terminal method with a gate control of carrier density in the junction. We measure the differential resistance of the fabricated CJJs using a standard lock-in technique in a He3 refrigerator, at a base temperature of 0.3 K.

Figure 1(c) shows the dV/dI as a function of DC bias current at several gate voltages V_g. $dV/dI = 0$ Ω indicates the supercurrent flowing from the inner to the outer Al. The bias current where the dV/dI starts to finitely increase from 0 Ω gives the switching current at each V_g. As V_g becomes more negative, the switching current decreases and finally vanishes. This implies that the supercurrent flows through the InAs quantum well and the gate control of the CJJ is achieved. We note that the product of the critical current and the normal resistance is approximately 15 μV, which is less than the typical value in the epitaxial Al Josephson junctions [24]. The Al/InAs interface can be degraded in our fabrication process without a protection layer such as the atomic layer deposition (ALD) grown Al$_2$O$_3$ layer but not too much to make the Josephson current strange.

We applied an out-of-plane magnetic field, B, to the CJJs and swept from -6 to 9 mT and back to -6 mT while

measuring dV/dI as a function of bias current. Figure 2 shows dV/dI as a function of B and bias current at some V_g when B is swept from 9 to -6 mT, and from -6 to 9 mT. The size of the supercurrent regions corresponding to the blue regions in Fig. 2 is reduced as V_g decreases because the switching current decreases as the carrier density decreases. Comparing the two panels obtained at the same V_g but opposite B sweep direction, we notice that the supercurrent regions approximately exhibit a right-triangle configuration, which is antisymmetric with respect to the line of $B = 0$ mT. This means that Fig. 2 indicates the sudden appearance of a resistance on the right and left of the $B = 0$ mT in the right and left panels, respectively.

When there is a finite number of vortices in the CJJ, the flow resistance is generated. Correspondingly, dV/dI is expected to be 0 when no vortices are embedded in the CJJ. As the vortex number increases, the flow resistance also increases and finally saturates to the normal resistance. Thereafter, we anticipate that the supercurrent region will be defined by a magnetic field to generate one flux quantum in the junctions; however, the magnetic field width of the supercurrent region in Fig. 2 is significantly larger than 0.6 mT, which corresponds to one flux quantum calculated from the junction area. This implies that the vortices existing in the CJJ are strongly trapped and cannot be driven by the electric current in case
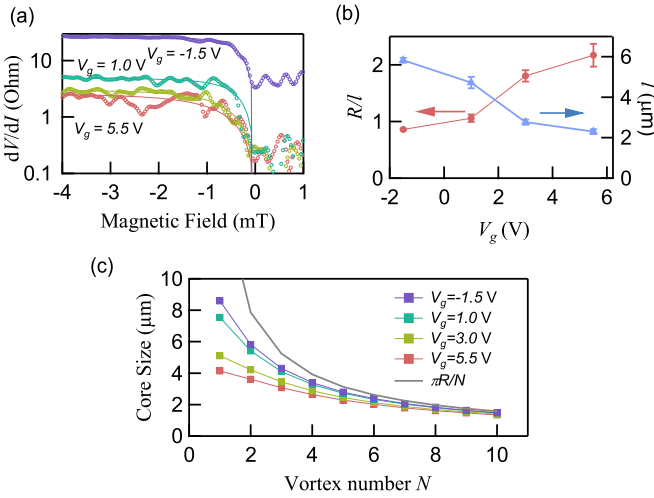
FIG. 3. (a) dV/dI versus magnetic field without bias current. The solid lines represent the numerical calculation results. (b) Evaluated R/l and l as a function of V_g: red circles for R/l (left axis) and blue triangles for l (right axis), respectively. (c)The core size as a function of vortex number N evaluated at different gate voltages. A larger N or V_g corresponds to a smaller core size.

of $B > 0.6$ mT when the field is swept from the positive to the negative, and $B < -0.6$ mT in the opposite sweep. We attribute this hysteresis to inductance of the outer superconductor. The inductance prevents the flux from moving out or in the superconducting loop. The hysteresis can then occur as well as the rf SQUID (Superconducting QUantum Interference Device). The inductance changes only the transition point where the fluxes exit or enter.

We now focus on the rise of dV/dI. For the understanding of further details, we indicate the line profiles of dV/dI versus B swept from $B = 9$ mT to $B = -6$ mT with no bias current in Fig. 3(a). Purple, green, yellow, and red circles of Fig. 3(a) correspond to the experimental results of dV/dI at $V_g = 5.5, 3.0, 1.0$, and -1.5 V, respectively. For clarity, the results are presented as a semilog plot. The sudden rise of dV/dI can be recognized at $B < 0$ mT for all the curves. In addition, as V_g increases, the slope of the sudden rise becomes steeper. The fine fluctuation on all traces of Fig. 3(a) can be assigned to the effect of trapped flux or Pearl vortex [28].

Here, we introduce a theoretical model for the flow resistance of the vortices in the CJJ [14]. The finite resistance can be given by

$$dV/dI = r_n/\sqrt{1 + (R/Nl)^2}, \quad (1)$$

with resistance r_n in the normal state, radii $R = 5$ μm of the CJJ, and the vortex number N [14]. Here, l is an important parameter to characterize the spatial variation of the gauge-invariant phase in the CJJ, and therefore, to determine the core size. According to the theoretical paper [14], the core size, R_{core}, can be calculated as

$$R_{core} = \frac{4R}{N} \arctan\left(\sqrt{1 + \left(\frac{R}{Nl}\right)^2} - \frac{R}{Nl}\right). \quad (2)$$

In the limit of $Nl \ll R$, the core size R_{core} is approximately obtained as $2l$, implying that the core is so small that there is

no dependence on N and R. Meanwhile, R_{core} is approximately $\pi R/N$ in the limit of $Nl \gg R$. In this case, the core size is determined by the circumference length divided by the number of embedded vortices, which implies that the vortices overlap among themselves.

This representation is only appropriate when the Pearl length, i.e., the penetration depth in a thin superconductor, is longer than R. In our CJJ, the junction region is not directly connected to the Al electrodes, but coupled to the proximity region which is the InAs quantum well beneath the Al electrodes. The superconducting properties in the junction between the proximity regions is characterized by proximity-induced superconductivity. Therefore, we calculated the Pearl length of the proximity-induced superconductivity and obtained $\Lambda = 2m/\mu_0 n e^2 = 170$ μm with InAs effective mass m and elementary charge e [29]. μ_0 is the vacuum permeability. We note that this Λ is long compared to R, implying that the model for the flow resistance in the CJJs can be applied in our experiment.

We note that the magnetic field induced in the CJJ should be quantized because the circular junction is surrounded by the outer superconducting electrode. Therefore, the flow resistance versus magnetic field plot should follow a step function, corresponding to the one-by-one entry of vortices. Meanwhile, the measured results in Fig. 3(a) do not show such step-shaped dependence. We infer that this is because the fluctuation assigned to a fingerprint of the Pearl vortices hides the expected step-shaped dependence. Therefore, we approximate Eq. (1) using $B = N\Phi_0/S$. $S = 0.1$ μm $\times$ $\pi \times 10$ μm is the area of the circular junction, resulting in $dV/dI = r_n/\sqrt{1 + (\frac{R\Phi_0}{lSB})^2}$. Φ_0 is a magnetic flux quantum $h/2e$. We performed the numerical fitting with r_n and R/l as free parameters. The calculated results presented as solid lines in Fig. 3(a) reproduce well the experimental results for $B < 0$ mT. The evaluated R/l and l are indicated as red and blue squares in Fig. 3(b), respectively. R/l decreases and l increases as V_g reduces, as expected, because l is written as $\Phi_0 R/2\mu_0 \Lambda I_c$ [14] and I_c decreases for the reduced V_g [see Fig. 1(c)]. In Fig. 3(b), R/l is 2.2 and l is 2.3 μm at $V_g = 5.5$ V.

We evaluate the core size R_{core} by substituting the estimated l at some V_g into Eq. 2. The evaluated core sizes as a function of N are plotted as the squares in Fig. 3(c). The core size in the limit of $R \ll Nl$ (equal to $\pi R/N$) is also represented in Fig. 3(c) as the gray line. The core size is always less than $\pi R/N$. A smaller gate voltage results in a longer core size because a longer l gives $R_{core} \propto 1/N$ and a shorter l weakens the dependence on N. As the core size approaches $\pi R/N$, the vortices begin overlapping among themselves. According to the theoretical paper [14], the shape of the vortex will be extended in the circumferential direction.

We fabricated and measured another CJJ device using the same geometry. Figure 4(a) indicates the dV/dI as a function of the bias current and magnetic field with opposite sweep directions and at various temperatures $T = 0.3, 0.5, 0.7$, and 0.9 K. We tuned V_g such that the switching current at $T = 0.3$ K assumes a similar value (about 3 μA) to that in the first device at $V_g = 5.5$ V. We observed similar features to those
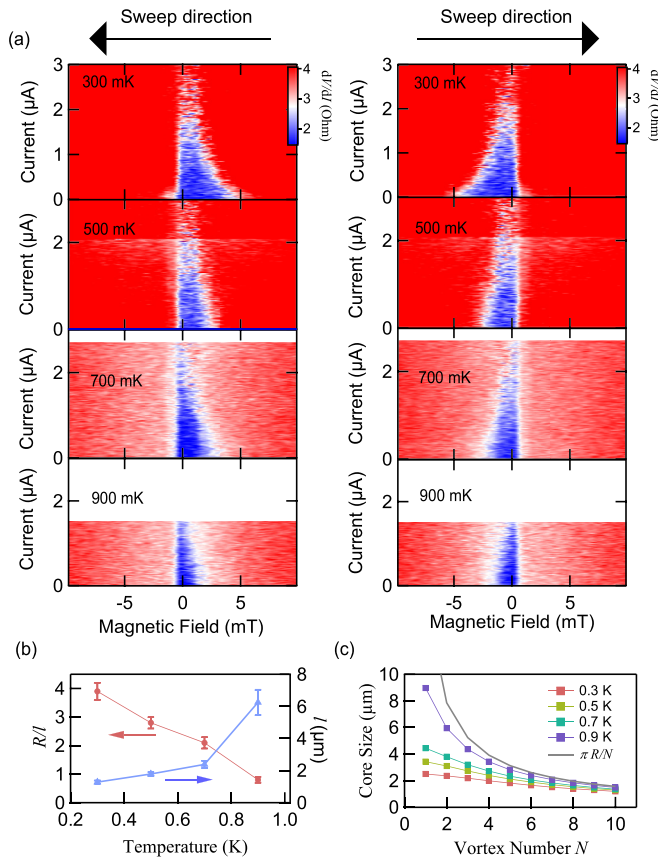
FIG. 4. (a) dV/dI as a function of magnetic field and bias current obtained at $T = 0.3, 0.5, 0.7,$ and 0.9 K. (b) R/l and l as a function of T: red circles for R/l (left axis) and blue triangles for l (right axis), respectively. (c)The core size as a function of vortex number N evaluated at various temperatures. A larger T corresponds to a bigger core size.

From the obtained parameter, we estimate the core size as a function of N at 0.3, 0.5, 0.7, and 0.9 K and plot it in Fig. 4(c). The core size at 0.3 K is significantly less than $\pi R/N$ and less dependent on N, reflecting the short l compared to R. Therefore, we notice that the vortices in $N < 4$ or 5 are localized at one point and do not spread in the entire CJJ. On the contrary, the vortices at 0.9 K seem to overlap among themselves.

Our results indicate that R/l can be controlled by V_g and T, i.e., we can control the core size and the degree of vortex overlap. Next, for making the well-localized vortices, i.e., well isolated MFs in the CJJ of topological insulators, higher carrier density, and lower temperature are required. This knowledge will be useful in designing the CJJ device for the demonstration of the MF braiding. In addition, we used very thin Al films as superconducting electrodes for making a high quality interface. However, Pearl vortices can readily be induced in the thin Al layer and the effect would be included in our results. Therefore, it is anticipated that the step function behavior of dV/dI as a function of the magnetic field may be obtained in the CJJ with thicker Al films.

In summary, we fabricated the gate-tunable CJJs from a wafer of epitaxial Al on an InAs quantum well. We observed the supercurrent through the CJJs, and we succeeded in the gate control. We found that the magnetic field dependence is triangular shaped with significant hysteresis against the sweep direction. In addition, we observed a finite resistance suddenly emerging from zero resistance in the supercurrent region as the field is swept. We explained the rise of the resistance with a theoretical model for the flow resistance of the vortices in the CJJs. From the analysis of the model, we estimated the vortex core size which becomes larger as V_g decreases and T increases. These results demonstrate that the core size is controlled by gate voltage and temperature. This paper gives essential information and methods for future studies of the Josephson vortices in the CJJs.

in Fig. 2, such as the supercurrent region shaped as a right triangle with a huge hysteresis and the sudden appearance of resistance assigned to flow resistance of the Josephson vortices [see Figs. 2 and 3(a)]. As T increases, the supercurrent region shrinks as shown in Fig. 4(a). In a similar manner as performed for the first device in Fig. 3(b), we estimated R/l and l at each temperature. The obtained R/l and l versus T is shown by the red and blue squares in Fig. 4(b). As T increases, l becomes longer. For example, l is $1.3 \, \mu$m at $T = 0.3$ K which is less than R.

[1] B. Josephson, Phys. Lett. **1**, 251 (1962).

[2] M. Tinkham, *Introduction to Superconductivity* (McGraw Hill New York, 1996).

[3] J. M. Rowell, Phys. Rev. Lett. **11**, 200 (1963).

[4] J. C. Cuevas and F. S. Bergeret, Phys. Rev. Lett. **99**, 217002 (2007).

[5] U. Ledermann, A. L. Fauchère, and G. Blatter, Phys. Rev. B **59**, R9027 (1999).

[6] D. Roditchev, C. Brun, L. Serrier-Garcia, J. C. Cuevas, V. H. L. Bessa, M. V. Milosevic, F. Debontridder, V. Stolyarov, and T. Cren, Nat. Phys. **11**, 332 (2015).

[7] A. Abrikosov, J. Phys. Chem. Solids **2**, 199 (1957).

[8] L. Fu and C. L. Kane, Phys. Rev. Lett. **100**, 096407 (2008).

[9] X.-L. Qi and S.-C. Zhang, Rev. Mod. Phys. **83**, 1057 (2011).

[10] S. R. Elliott and M. Franz, Rev. Mod. Phys. **87**, 137 (2015).

[11] J.-P. Xu, M.-X. Wang, Z. L. Liu, J.-F. Ge, X. Yang, C. Liu, Z. A. Xu, D. Guan, C. L. Gao, D. Qian, Y. Liu, Q.-H. Wang, F.-C. Zhang, Q.-K. Xue, and J.-F. Jia, Phys. Rev. Lett. **114**, 017001 (2015).

[12] H.-H. Sun and J.-F. Jia, npj Quantum Materials **2**, 34 (2017).

[13] R. H. Hadfield, G. Burnell, D.-J. Kang, C. Bell, and M. G. Blamire, Phys. Rev. B **67**, 144513 (2003).

[14] J. R. Clem, Phys. Rev. B **82**, 174515 (2010).

[15] E. Grosfeld and A. Stern, Proc. Natl. Acad. Sci. USA **108**, 11810 (2011).

[16] S. Park and P. Recher, Phys. Rev. Lett. **115**, 246403 (2015).

[17] S. Park, H.-S. Sim, and P. Recher, arXiv:1812.09573.

[18] V. V. Dremov, S. Y. Grebenchuk, A. G. Shishkin, D. S. Baranov, R. A. Hovhannisyan, O. V. Skryabina, N. Lebedev, I. A. Golovchanskiy, V. I. Chichkov, C. Brun, T. Cren, V. M. Krasnov, A. A. Golubov, D. Roditchev, and V. S. Stolyarov, Nat. Commun. **10**, 4009 (2019).

[19] J. Yan and M. S. Fuhrer, Nano Lett. **10**, 4521 (2010).

[20] K. Chida, T. Hata, T. Arakawa, S. Matsuo, Y. Nishihara, T. Tanaka, T. Ono, and K. Kobayashi, Phys. Rev. B **89**, 235318 (2014).

[21] M. J. Zhu, A. V. Kretinin, M. D. Thompson, D. A. Bandurin, S. Hu, G. L. Yu, J. Birkbeck, A. Mishchenko, I. J. Vera-Marun, K. Watanabe, T. Taniguchi, M. Polini, J. R. Prance, K. S. Novoselov, A. K. Geim, and M. B. Shalom, Nat. Commun. **8**, 14552 (2017).

[22] Y. Zeng, J. I. A. Li, S. A. Dietrich, O. M. Ghosh, K. Watanabe, T. Taniguchi, J. Hone, and C. R. Dean, Phys. Rev. Lett. **122**, 137701 (2019).

[23] M. Kjaergaard, F. Nichele, H. J. Suominen, M. P. Nowak, M. Wimmer, A. R. Akhmerov, J. A. Folk, K. Flensberg, J. Shabani, C. J. Palmstrom, and C. M. Marcus, Nat. Commun. **7**, 12841 (2016).

[24] M. Kjaergaard, H. J. Suominen, M. P. Nowak, A. R. Akhmerov, J. Shabani, C. J. Palmstrøm, F. Nichele, and C. M. Marcus, Phys. Rev. Appl. **7**, 034029 (2017).

[25] J. S. Lee, B. Shojaei, M. Pendharkar, A. P. McFadden, Y. Kim, H. J. Suominen, M. Kjaergaard, F. Nichele, H. Zhang, C. M. Marcus, and C. J. Palmstrøm, Nano Lett. **19**, 3083 (2019).

[26] See Supplemental Material at http://link.aps.org/supplemental/10.1103/PhysRevB.102.045301 for the carrier density estimation.

[27] S. Matsuo, K. Ueda, S. Baba, H. Kamata, M. Tateno, J. Shabani, C. J. Palmstrøm, and S. Tarucha, Sci. Rep. **8**, 3454 (2018).

[28] See Supplemental Material at http://link.aps.org/supplemental/10.1103/PhysRevB.102.045301 for the detailed discussion.

[29] See Supplemental Material at http://link.aps.org/supplemental/10.1103/PhysRevB.102.045301 for Pearl length estimation.